DSM AND DTM GENERATION FROM VHR SATELLITE STEREO IMAGERY OVER PLASTIC COVERED GREENHOUSE AREAS

Abderrahim Nemmaoui*[a], Fernando J. Aguilar [a], Manuel A. Aguilar [a], Rongjun Qin [b,c]

* Corresponding author: an932@ual.es

[a] Department of Engineering, University of Almería, Ctra. de Sacramento s/n, La Cañada de San Urbano, Almería 04120, Spain (an932@ual.es, faguilar@ual.es, maguilar@ual.es)

[b] Department of Civil, Environmental and Geodetic Engineering, The Ohio State University, 218B Bolz Hall, 2036 Neil Avenue, Columbus, OH 43210, USA (qin.324@osu.edu)

[c] Department of Electrical and Computer Engineering, The Ohio State University, Dresse Lab 205, 2015 Neil Avenue, Columbus, OH 43210, USA

Abstract

Agriculture under Plastic Covered Greenhouses (PCG) has represented a step forward in the evolution from traditional to industrial farming. However, PCG-based agricultural model has been also criticized for its associated environmental impact such as plastic waste, visual impact, soil pollution, biodiversity degradation and local runoff alteration. In this sense, timely and effective PCG mapping is the only way to help policy-makers in the definition of plans dealing with the trade-off between farmers' profit and environmental impact for the remaining inhabitants.

This work proposes a methodological pipeline for producing high added value 3D geospatial products (Digital Surface Models (DSM) and Digital Terrain Models (DTM)) from VHR satellite imagery over PCG areas. The 3D information layer provided through the devised approach could be very valuable as a complement to the traditional 2D spectral information offered by VHR satellite imagery to improve PCG mapping over large areas.

This methodological approach has been tested in Almeria (Southern Spain) from a WorldView-2 VHR satellite stereo-pair. Once grid spacing format DSM and DTM were built, their vertical accuracy was assessed by means of lidar data provided by the Spanish Government (PNOA Programme).

Regarding DSM completeness results, the image matching method based on hierarchical semi-global matching yielded much better scores (98.87%) than the traditional image matching method based on area-based matching and cross-correlation threshold (86.65%) when they were tested on the study area with the highest concentration of PCG (around 85.65% of PCG land cover). However, both image matching methods yielded similar vertical accuracy results in relation to the finally interpolated DSM, with mean errors ranging from 0.01 to 0.35m and random errors (standard deviation) between 0.56 and 0.82 m. The DTM error figures also showed no significant differences between both image matching methods, although being highly dependent on DSM-to- DTM filtering error, in turn closely related to greenhouse density and terrain complexity.

KEYWORDS: Digital Elevation Model, Digital Surface Model, Greenhouse land cover, VHR satellite stereo imagery, Stereo image matching.

1. Introduction

Since the first use of plastic film in agriculture in 1948 (Garnaud, 2000), plastic covering has been used extensively in the cultivation of vegetables around the world. Particularly, plastic covered greenhouses (PCG) can be considered a step forward in the evolution from traditional to industrial farming (i.e. from extensive to intensive farming). PCG present a cover made of transparent plastic film to control the environmental conditions and growth of the crops growing inside. This leads to a significant crop yield increasing under highly controlled growing conditions. For these reasons, greenhouse farming plays an increasing role in modern agriculture, becoming one of the most important agricultural activities in arid and semi-arid regions. Crops under PCG accounted for a total coverage of about 3019 million hectares worldwide in 2016, mainly located in Europe (Mediterranean areas), North Africa, the Middle East and China (Wu et al., 2016). In these areas, PCG increase day by day, thus obtaining timely and accurate information regarding their spatial distribution could make an important contribution to local agricultural management, environmental protection and land use/land cover (LULC) policy.

LULC changes can directly affect the status and integrity of ecosystems. For instance, natural and multifunctional landscapes can be converted into areas of intensive farming, altering the main land-use type and natural character of a region. This is the case of Almeria, south-eastern Spain, a region that is currently hosting the largest concentration of greenhouses in the world, spread across more than 30000 hectares, and being locally known as “The Plastic Sea of Almeria” (Aguilar et al., 2015). The region has undergone major LULC changes over the preceding decades due to the expansion of intensive greenhouse horticulture, making the area one of the most economically prosperous in the country.

Furthermore, ecosystems in south-eastern Spain are high in biodiversity and are, because of their location in the driest region in continental Europe, vulnerable to global change impacts. In this sense, management decisions should promote a transition towards sustainable landscape strategies which result in human needs being satisfied while simultaneously maintaining important ecological processes responsible for the delivery of ecosystem services (Quintas-Soriano et al., 2016). This transition requires a thorough knowledge of PCG spatio-temporal distribution where remote sensing seems to be the only feasible approach for understanding its impacts on climate and eco-environment in a large geographic area. In fact, remote sensing can efficiently provide quantitative and qualitative information of great interest for the study of planning, land organization and sustainable development of this kind of extremely complex agro-systems (Aguilar et al., 2007).

However, PCG spectral-based mapping from remote sensing turns out to be challenging because the spectral signature of the plastic-covered greenhouse can change drastically (Aguilar et al., 2015, 2014a; Tarantino and Figorito, 2012). In fact, different plastic materials with varying thickness, transparency, ultraviolet and infrared reflection and transmission properties, additives, age and colours are used in greenhouse coverings (M. A. Aguilar et al., 2016). Moreover, as plastic sheets are semi-transparent, the changing reflectance of the crops underneath them affects the greenhouse spectral signal reaching the sensor (Levin et al., 2007). Finally, such plastic materials occasionally yield specular reflections that create shiny spots that are particularly challenging for the extraction of their corresponding 3D surface geometry from overlapping digital images acquired from multiple views, a widely known computer vision approach named digital image matching.

Regarding PCG mapping from remote sensing approaches, an increasing scientific literature has emerged during the last decade. A comprehensive literature review can be found in Aguilar et al. (2015), M. A. Aguilar et al. (2016), Celik and Koc-San (2018), Lanorte et al. (2017), Novelli et al. (2016) and Yang et al. (2017), showing that many researchers have tried to improve the accuracy of PCG mapping by applying both pixel-based and object-based supervised image classification algorithms to high and medium resolution satellite imagery and by means of both static and multi-temporal approaches, reporting overall accuracies ranging between 85% and 94%. Nowadays it is difficult to overcome those scores without adding new information (i.e. in addition to spectral and texture features) to the features vector employed to feed the classifier.

On the other hand, nowadays geospatial analysis headed up to mapping complex above-ground features (e.g. built-up areas) are emerging, usually requiring digital surface and terrain modelling to produce Digital Surface Models (DSM), which capture the natural and built-up features on the Earth's surface, and Digital Elevation Models (DEM), which are able to characterize the topography or bare-earth elevation (Li et al., 2005). Both geospatial products have proven to be relevant in several agricultural applications (Celik and Koc-San, 2018; Mokarram and Hojati, 2017; Seeruttun and Crossley, 1997) .

The so-called normalized digital surface model (nDSM) is generated by computing the difference between the DSM and the DEM. Since the nDSM excludes the influence of topography, it represents the height of all overlying objects on the terrain, such as buildings, trees and greenhouses. In this way, several researchers have proposed to incorporate this 3D information as a raster layer to improve the overall accuracy classification and extraction of man-made features on built-up areas (Aguilar et al., 2014b; Luethje et al., 2017; Weidner and Förstner, 1995; Zhang et al., 2015). Recently nDSM have been also used to derive the 3D properties of urban buildings, which represent the three-dimensional nature of living spaces and are needed in population estimation or urban planning (Tomas et al., 2016).

At the same time, the launching of many Very High Resolution (VHR) satellites capable of capturing panchromatic imagery with Ground Sample Distance (GSD) lower than 1 m has opened the greatest possibilities for cartographic applications based on the extraction of DSM and DEM. These products are generated by image matching strategies from VHR satellite imagery stereo pairs or stereo triplets. Current stereo capabilities of VHR satellites, together with their agile pointing ability, enable the generation of geometrically robust (in terms of base-to-height ratio) and radiometrically consistent along-track stereo images which can be acquired for any place on Earth (Zhang and Gruen, 2006; Büyüksalih and Jacobsen, 2007a.; D'angelo et al., 2008; Dowman et al., 2012; Poli and Caravaggi, 2012; Aguilar et al., 2014b). In this sense, space-borne images provide a cost-efficient alternative to aerial images and can be obtained regardless of various national over-flight restrictions. Furthermore, their appropriate stereo geometry and radiometric similarity allow obtaining high resolution DSM by i) carrying out an aerotriangulation and bundle adjustment process based on object-to-image geometry provided by the well-known rational polynomial coefficients (RPC) (Grodecki and Dial, 2003), and ii) generating a DSM from applying automatic stereo matching procedures over previously epipolarly rectified stereo images (e.g. Alobeid et al., 2010). Since RPC are generated without ground data, it is necessary to improve satellite imagery orientation for high accuracy applications by measuring ground control points (GCP) and computing bias-corrected RPC (Aguilar et al., 2013; Tong et al., 2010). Aguilar et al. (2017) have recently developed an approach for improving the initial direct geolocation accuracy of VHR satellite imagery based on the extraction of 3D GCP from freely available ancillary data at global coverage such as multi-temporal information of Google Earth and the Shuttle Radar Topography Mission 30 m digital elevation model. This approach can be very useful when ground surveyed control points are not available.

There is available an abundant literature about the use of VHR satellite or aerial imagery for DSM generation. For instance, the reader can find a complete and comprehensive overview of the characteristics and use of VHR satellite and aerial images in (Dowman et al., 2012). Concerning the radiometric and geometric quality of VHR satellite imagery, while the earlier studies were based on slightly coarser spatial resolution (>0.5 m Ground Sample Distance (GSD)) (e.g. Büyüksalih and Jacobsen, 2007a; D 'angelo et al., 2008; Toutin, 2006a; Toutin et al., 2001; Zhang and Gruen, 2006), the last investigations have been mainly focused on VHR satellites with GSD even lower than 0.5 m, such as GeoEye-1 and WorldView-1/2/3/4 (Åstrand et al., 2012; Barbarella et al., 2017; Capaldo et al., 2012b; Reinartz et al., 2014), and the capabilities of the PAN triplet product from Pléiades-1 to generate DSMs (Fratarcangeli et al., 2016; Poli et al., 2015; Tack et al., 2009). Other works were more focused on testing image matching algorithms (Alobeid et al., 2010; Capaldo et al., 2012a; de Franchis et al., 2014; Di Rita et al., 2017; Ghuffar, 2016; Noh and Howat, 2015; Qin, 2016; Shean et al., 2016; Wenzel et al., 2013). There are also several works about DSM generation from VHR satellite imagery over different types of land cover, including urban areas (Arefi and Reinartz, 2013; Büyüksalih and Jacobsen, 2007b; Dowman, 2000; Jacobsen, 2006; Muller et al., 1997; Sohn and Dowman, 2007; Tian et al., 2014), mountainous areas (Toutin, 2002), densely vegetated deciduous forest (DeWitt et al., 2017), glaciated regions (Noh and Howat, 2015) or over herb and grass land cover (Hobi and Ginzler, 2012). However, to the best of our knowledge, few works have been specifically focused on plastic covered greenhouse areas (Aguilar et al., 2014a; Celik and Koc-San, 2018; Aguilar et al., 2018).

The procedure for assessing digital elevation model (DEM) or DSM quality involves examination of the vertical accuracy and completeness (Butler et al., 1998; Höhle and Potuckova, 2006). Most of the current research uses highly accurate lidar information as ground truth to check the accuracy of DSMs generated from VHR satellite images (Capaldo et al., 2012a; Noh and Howat, 2017, 2015, Toutin, 2006b, 2006a). Considering that the automatic DSM cannot be obtained in all areas due to matching errors provoked by insufficient texture, occlusions or radiometric artifacts, DSM vertical accuracy should be complemented by DSM completeness, a DSM quality indicator defined as the percentage of correctly matched points over the working area (Höhle and Potuckova, 2006)

The main goal of this study is to develop and test a methodological approach to produce high quality DSM and DEM from WorldView-2 along-track stereo pair headed up to obtain 3D geospatial features. These 3D features could complement 2D spectral features in PCG mapping over large areas, as it has been already reported by Aguilar et al. (2014a) and Celik and Koc-San (2018). In this sense two software packages, based on two clearly different stereo image matching approaches, were tested with respect to their ability to produce photogrammetrically derived DSM/DEM over dense greenhouse covered areas.

The rest of this paper is organized as follows. The study area and datasets are described in the section 2. The third section outlines a detailed explanation of the methodological approach devised to produce high quality DSM and DEM from VHR satellite imagery and the pipeline used to assess the performance of the two stereo image matching approaches. The results corresponding to the completeness and characteristics of the residual populations for the stereo-photogrammetrically derived DSM and DEM are presented and discussed in the section 4. Conclusions are provided in the last section.

2. Study Site and Datasets

2.1. Study area

The study area is located in the province of Almeria (Southern Spain), housing the greatest concentration of greenhouses in the world. It comprised a rectangle area of about 8000 ha centred on the WGS84 geographic coordinates of 36.7824°N and 2.6867°W (Fig. 1).

This pilot area presents an elevation ranging between 152.6 m and 214.8 m above mean sea level (Spanish orthometric heights EGM08-REDNAP), with a moderate north-south mean slope of around 4.3%.

Fig. 1. Location of the study site in the province of Almeria (Spain) and the four selected subareas as red rectangles. These subareas are characterized, in addition to PCG, by features such as dry ravines (1), vegetation (2) urban areas (3) and very high concentration of PCG (4). Coordinate System: WGS84 UTM Zone 30.

Within the study area, four representative rectangular test areas of 920 m x 620 m were selected, including different land covers and features such as dry ravines and bare soil (test area 1), vegetation and bare soil (test area 2), urban areas (test area 3) and a variable density of PCG land cover which reaches the highest density in the fourth test area (test area 4) (Fig. 1).

2.2. WorldView-2 stereo pair

A WorldView-2 (WV-2) along-track stereo pair taken on July 5, 2015, was used. It consisted of 2 Level-2A images (ORS2A) format, dynamic range of 11-bit (without dynamic range adjustment) and 0.5 m GSD (PAN). The off-nadir angle for the two stereo pair images turned out to be 12.6° and 24.6° (Table 1).

Table 1 Characteristics of the panchromatic band for the WV-2 stereo pair.

2.3. Ground truth lidar data

The lidar data used as ground truth in this study were provided by the PNOA (National Plan of Aerial Orthophotography of Spain) as RGB coloured point cloud in LAS binary file, format v. 1.2, containing easting and northing coordinates (UTM ETRS89 30N) and orthometric elevations (geoid EGM08-REDNAP). It was taken on September 23, 2015, by means of a Leica ALS60 discrete return sensor with up to four returns measured per pulse and an average flight height of 2700 m. The nominal average point density of the lidar campaign was 0.7 points/m^2, although the finally registered point density of the test area, considering overlapping, turned out to be 0.97 points/m^2 (all returns). The nominal nadiral horizontal accuracy ($RMSE_{xy}$) and nominal vertical accuracy ($RMSE_z$) after processing took values lower than 0.3 m and 0.2 m, respectively (Ministerio de Fomento de España, 2015). The 131 GPS-RTK surveyed GCP were employed to check the nominal vertical accuracy of lidar data. The standard deviation of the computed lidar vertical error, only including open terrain GCP (Aguilar et al., 2008), took a value of 0.14 m, which mean a vertical accuracy higher than the 0.2 m nominal vertical error of PNOA lidar data.

A local maxima filter algorithm with 2 m neighbourhood size to search for maximum height was applied to the lidar point cloud to obtain the corresponding lidar-derived point cloud DSM. Additionally, a lidar-derived point cloud DEM was produced by automatically filtering ground points using the Improved Progressive TIN Densification (IPTD) filtering algorithm proposed by Zhao et al. (2016). The corresponding IPTD set of parameters was optimized for each test area. The automatically classified ground points were manually edited to achieve a final high-quality point cloud DEM.

The lidar-derived point cloud DSM and DEM were finally interpolated to 1 m grid spacing by using the Gaussian Markov Random Field (GMRF) algorithm, following the procedure and the mathematical framework described and tested by F. J. Aguilar et al. (2016). (The cited paper and the GMRF interpolation method code are freely available at https://github.com/3DLAB-UAL/dem-gmrf Link to code). In this work the GMRF interpolation method was tested in the same study area providing good results. As an advantage, the GMRF mathematical framework makes possible to both retrieve the estimated uncertainty for every interpolated elevation point and include break lines or terrain discontinuities between adjacent cells to produce high-quality DEMs.

The lidar-derived grid format DSM and DEM depicted in Fig. 2 were employed as ground truth for the vertical accuracy assessment of the stereo-photogrammetrically extracted DSM and DEM corresponding to the four test areas.

Fig. 2. Lidar-derived grid format DSM and DEM for the four test areas. Left column: Lidar-derived DSM. Right column: Lidar-derived DEM. The red line (DEM test area 1 in the first row on the right) corresponds to the location of the profile represented in Fig. 7).

3. Methods

The methodological pipeline proposed in this work to provide 3D information potentially useful to improve PCG mapping over large areas from VHR satellite stereo imagery is described in this section. It consisted of the steps shown below.

3.1. Step 1: Stereo photogrammetrically derived DSM

Two different software packages, based on two clearly different types of image matching approaches, were used to stereo-photogrammetrically generate the DSM from

WV-2 imagery.

PCI Geomatics v. 2016 (PCI Geomatics, Richmond Hill, ON, Canada) was the first software tested. This software has been chosen in several studies and works (i.e. Barbarella et al., 2017; Capaldo et al., 2012a; Di Rita et al., 2017a) as benchmark for others software packages in comparison tests.

PCI Geomatics (PCI henceforth) implements a photogrammetric tool called OrthoEngine devised to produce geospatial products. The OrthoEngine matching algorithm is based on cross-correlation where an automated area-based matching procedure is performed on quasi-epipolar images. Specifically, this procedure is based on a hierarchical (seven steps) sub-pixel mean normalized cross correlation matching method that generates correlation coefficients between zero and one for each matched pixel, meaning zero a total mismatch and one a perfect match. When the correlation coefficient of a matched point is lower than 0.5, this point is rejected, and its height is not computed, meaning a gap and reducing the DSM completeness. Finally, a second-order surface is then fitted around the maximum correlation coefficients to find the match position to sub-pixel accuracy (Cheng, 2015).

The other tested software was RPC Stereo Processor (RSP), initially developed by Qin, (2014) for 3D change detection and land cover classification studies. It was further refined as a standalone software package that performs stereo matching on RPC modelled space-borne images producing mapping products such as DSM and orthophoto (Qin, 2016). RSP implements a hierarchical semi-global matching (SGM) approach based on the widely known algorithm proposed by Hirschmuller, (2008) to generate the disparity maps after applying an epipolar rectification process to the original stereo images. Note that the classic SGM creates a raster file to store the aggregated cost for each disparity value, thus requiring a lot of memory for computation. Hence RSP provides a hierarchical solution based on running the classic SGM algorithm through pyramid image layers. At the same time, RSP restrains the disparity search in the original resolution within a given range (e.g. [-1000, 1000]) in order to retain high resolution in the coarsest layer of the pyramids (Qin, 2016).

The initial vendor supplied RPC set, derived from satellite ephemeris and star tracker observations, usually contains bias that should be corrected for precise epipolar image generation. A first order affine transformation (six parameters) on the image space was used to obtain bias-corrected RPC at the RPC-based satellite image orientation stage both in the case of PCI and RSP pipelines. Following the recommendations of Åstrand et al., (2012) and Aguilar et al., (2013), 7 GPS-RTK ground points evenly distributed over the working area were selected as GCP. The remaining 124 ground points were used as Independent Check Point (ICP). The planimetric accuracy ($RMSE_{2D}$) of the image orientation phase measured at those ICPs was 0.45 m. It is important to keep in mind that the GCP were only marked once on the image space of the PCI project, being later exported to be automatically marked in the RSP project to assure the same conditions at the satellite image orientation phase.

After carrying out the sensor orientation phase, 1 m grid spacing DSM was stereo-photogrammetrically extracted from each one of the two tested approaches. In the case of PCI, hilly terrain and without filling blanks (no interpolation) parameters were chosen. In the case of the RSP software, the DSM was also extracted without filling blanks.

3.2. Step 2: DSM outlier removal

Potential outliers were automatically removed from the original DSM (presenting blank areas) by adapting the parametric statistical method for DEM error detection published by Felicísimo, (1994). This algorithm takes advantage of probabilistic criteria to apply a parametric procedure based on the assumption that differences between the height of every point and its corresponding neighbourhood mean height follows a normal distribution. In our case, the neighbourhood size was set to 1.5 times the DSM grid spacing.

Once potential outliers were removed (outlier-corrected DSM), the GMRF interpolation method described in F. J. Aguilar et al. (2016) was employed to fill the blank areas and produce a continuous 1 m grid spacing DSM (GMRF DSM) .

3.3. Step 3: Automatic DEM extraction from the outlier-corrected DSM

It is beyond the scope of this work to compare the results provided by the various available algorithms focused on 3D data filtering to automatically convert a DSM into a bare-earth DEM because of most of these algorithms have been developed to deal with high vertical accuracy lidar point clouds. Therefore, their performance on photogrammetrically derived 3D point clouds from VHR satellite imagery should be carefully tested. In this way, the easy-to-use algorithm (only two parameters to tune) called DSM2DTM, implemented in PCI Geomatics, was employed to automatically extract the corresponding DEM from the outlier-corrected DSM obtained in the step 2. This algorithm is able to convert a DSM into a bare-earth DEM by obtaining local area minimum/maximum values and then operating a moving polynomial function utilizing the local values in the specified object size parameter (PCI Geomatics, 2016).

The DSM2DTM algorithm was launched by using an iterative python code with two varying parameters to search for an optimal output DEM in each test area. Those parameters were the following:

i) Object size, with values ranging from 50 m to 200 m depending on the morphology of each test area and the image matching algorithm. It specifies the size of the filters which are used to remove surface features. Typically, the size should be as large as the largest feature (e.g. greenhouse) that should be removed.

ii) Gradient percentage threshold (slope), with values ranging from 5% to 35% depending on the morphology of each test area and the image matching algorithm. Features with slopes less than this threshold will be treated as natural features and will not be removed. The type of terrain selected was “Hilly” in all cases.

Finally, a 1 m grid spacing DEM was built from the automatically filtered terrain points provided by the DSM2DTM algorithm by applying the GMRF interpolation method (F. J. Aguilar et al., 2016).

3.4. Quality assessment of the extracted GMRF DSM and DEM

The quality of the extracted GMRF DSM and the derived DEM was assessed by computing their completeness and vertical accuracy. In order to study the influence of the dominant land cover on the aforementioned quality indicators, the quality assessment was carried out over the four test areas previously described and depicted in Fig. 1. In each case, the corresponding lidar-derived DSM and DEM were used as ground truth, computing residuals as photogrammetric height minus lidar height.

The completeness of every DSM was computed for every test area as the ratio between the blank areas (number of missing image matching points) and all the DSM 1 m grid spacing points which should have been potentially extracted.

The vertical accuracy statistics of each GMRF DSM and DEM were separately computed for each test area after applying the widely known 3σ rule (Daniel and Tennant, 2001) to remove blunder errors from the residuals populations (z-residuals). In this way, several statistics such as mean value, standard deviation and 90th (*LE90*) and 95th (*LE95*) percentile linear error were computed.

4. Results and discussion

4.1. DSM Completeness

The completeness scores of the DSM produced from PCI and RSP methods were significantly different. In fact, Fig. 3 depicts that the RSP-derived DSM showed a less number of missing image matching points than the one obtained from PCI, especially in those test areas where urban and PCG land cover were more abundant (test areas 3 and 4, respectively. See Fig. 1 and Fig. 3).

Fig. 3. Stereo photogrammetrically derived DSM corresponding to the four test areas generated from PCI (left column) and RSP (right column).

In the test area 1 (Fig. 3), containing bare soil and dry ravines as the more representative features, the RSP software reached a completeness higher than 99% compared to around 93% achieved by PCI (Table 2). In the case of the test area 2, which mainly presents bare soil and vegetation land covers, the completeness took values of 99.57% and 94.42% for the RSP and PCI methods, respectively. Regarding the test area 3, predominantly covered by PCG, urban areas and bare soil, the completeness reached a value of 99.25% in the case of the RSP method, offering a significantly lower value of 88.13% in the case of the PCI approach. In the very dense greenhouse covered area labelled as the test area 4, the completeness score of 98.87% provided by the RSP method clearly exceeded the value of 86.65% performed by the PCI method.

Table 2 PCG landcover density and completeness values for the DSM extracted from applying the RSP and PCI stereo-matching approaches.

From comparing the completeness results obtained in the four test areas, it can be stated that the higher the PCG landcover density, the lower the completeness score, especially in the case of PCI results. Indeed, the RSP method provided better results than the PCI one for the four test areas. The difference in completeness scores between RSP and PCI DSM reached the highest value (around 12%) in the test area 4, which had the biggest concentration of greenhouse landcover.

It is worth nothing that there is a clear relationship between missing matching points (low local DSM completeness) and the local radiometric dissimilarity over greenhouse plastic cover between the two overlapping satellite images. This finding can be made out in Fig. 4, where the DSM produced in the test area 4 from using PCI and RSP software packages are depicted together with the two VHR WV-2 PAN satellite images. The blue ellipses highlight greenhouses presenting important radiometric changes due to glint effect in one of the stereo pair images, thus causing matching problems in DSM production (red colour). However, when greenhouses presented extreme values of digital number because of they are painted white in summer to protect crops from excessive radiation and reduce the heat inside, the matching algorithm worked usually well. These painted greenhouses are marked by mean of yellow ellipses in Fig. 4, not presenting visible radiometric changes between the two stereo pair images.

Fig. 4. Influence of local radiometric dissimilarity on greenhouse plastic cover in relation to DSM completeness over the test area 4. The PAN images from WV2 stereo pair are shown above. DSM produced by PCI and RSP software packages are shown below. Blue ellipses highlight greenhouses presenting glint changes while yellow ellipses mark two greenhouses painted white. Matching problems in both DSM are presented in red colour.

4.2. Vertical accuracy

4.2.1. GMRF DSM vertical accuracy assessment

Table 3 shows the results for the GMRF DSM vertical accuracy assessment corresponding to each test area. In general, and regarding random errors assessment, the two tested satellite image matching methods performed quite similar, providing standard deviation and *L95* values ranging from 0.56 to 0.82 m and 1.34 to 2.10 m, respectively. The poorest vertical accuracies in terms of DSM random errors were obtained in the case of the test area 4, which presented the highest concentration of PCG.

In relation to systematic errors, the RSP approach showed a higher positive bias than the PCI one, thus slightly overestimating the reference z-values given by the lidar-derived DSM in all the test areas, but especially in the test areas 3 and 4 which housed the highest density of PCG (Table 2). In terms of linear error computed at 90% and 95% percentiles (*L90* and *L95*), the results provided by both RSP and PCI approaches can be considered as significantly similar, also rising with the increase of greenhouse land cover density.

Provided that RSP presented a higher completeness in DSM generation than PCI, their similar results from the vertical accuracy assessment in terms of random errors and a slightly higher bias in the case of RSP seem to point to the fact that RSP is incurring a commission error when working on difficult to match image areas (e.g. glint effect mentioned above). In other words, PCI matching method turns out to be more reluctant to accept pairs of matching points with weak similarity (measured through cross-correlation coefficient), therefore tending to leave more blank areas and so reducing completeness. On the contrary, RSP can compute the 3D position of those weak matching points, so improving the visual appearance of the compiled DSM but also increasing the probability of incurring vertical error. It is important to highlight that the GMRF interpolation algorithm was able to properly fill the DSM gaps left by PCI method, especially in greenhouse land cover areas, without significantly affecting the final vertical accuracy results, a finding already reported by F. J. Aguilar et al. (2016).

The spatial distribution of GMRF DSM errors is depicted in Fig. 5. The error distribution of RSP and PCI compiled GMRF DSM presented a similar pattern, with the highest vertical error mainly localized along manmade features edges. Most of errors are positive, i.e. stereo-photogrammetrically derived DSM slightly overestimated the true z-values provided by the lidar reference DSM. This was expected since photogrammetric points could be considered as the features visual envelope. Finally, most of the working area presented absolute errors lower than 1 m, which can be deemed an adequate result.

Table 3 Vertical accuracy assessment results for the GMRF DSM produced by the PCI and RSP stereo matching methods. Units expressed in meters.

Fig. 5. Spatial distribution of residuals for the GMRF DSM corresponding to the four test areas generated from PCI (left column) and RSP (right column).

4.2.2. DEM vertical accuracy assessment

With regards to the automatically filtered and GMRF interpolated DEM, the random errors, measured in terms of standard deviation, were similar for all the test areas and between the two image matching methods tested for DSM production (Table 4). As expected, the computed DEM standard deviation was consistently higher than that estimated in the case of GMRF DSM, ranging from 1.16 to 2.28 m. Indeed, now there are two concomitants sources of error, DSM original error and DSM-to-DEM error (DSM filtering error). However, the test area 1 showed the highest random error value, mainly due to the presence of two relatively deep dry ravines running from North to South.

Also note that the systematic errors depicted a different behaviour in the test area 1 compared to those observed in the other test areas. In fact, the mean error in the test area 1 presented a negative bias, thus underestimating the true elevation provided by the lidar derived DEM data. Just the opposite happened in the other test areas. This bias effect was again more pronounced in those DEM filtered from the DSM produced by RSP method, probably because RSP assumes more risk in image matching over cumbersome areas. In the vertical profile shown in Fig. 7, it can be appreciated that the filtered DEM extracted from the corresponding PCI generated DSM (similar behaviour was observed in the case of the RSP derived DEM) resulted in an excessively smooth surface along the dry ravine, producing a noticeable decrease in slope on its originally steep flanks and a subsequent underestimation of the elevations provided by the lidar-derived DEM. This undesirable effect was due to the way in which the algorithm DSM2DTM, implemented in PCI Geomatics, automatically converts a DSM into a bare-earth DEM by applying a series of filtering steps that remove features such as buildings, greenhouses and vegetation stands and, at the same time, maintain natural terrain features under a previously set slope threshold. Likely, the slope threshold parameter selected for the test area 1 (35%) should be increased to avoid filtering out the steep gully flanks. In any case, it is beyond the scope of this article to conduct an in-depth study about the optimization of the available DSM-to-DEM filtering algorithms. Only note that the use of spatially adapted parameters could notably improve the results regarding DEM accuracy.

Table 4 Vertical accuracy assessment results for the DEM extracted from the DSM produced by the PCI and RSP stereo matching methods. Units expressed in meters.

The spatial distribution of DEM residuals is shown in Fig. 6. As explained above, the test area 1 depicts a general underestimation of the true elevation values mainly located along the two steep flanks of the dry ravines. An opposite situation can be seen in the other test areas, where the general tendency would be more prone to overestimate DEM elevations, especially in greenhouse built-up areas. In fact, the higher the greenhouse density, the higher the positive bias in signed DEM residuals (Table 4). In the main, the DSM-to-DEM algorithm produced an insufficient removal of built-up features, especially greenhouses, as compared to the lidar derived DEM which may even register some last laser returns onto the greenhouse floor, thus contributing to a better definition of the bare-earth DEM.

Fig. 6. Spatial distribution of residuals for the DEM corresponding to the four test areas derived from PCI DSM (left column) and RSP DSMs (right column).

Fig. 7. Vertical profile crossing one of the dry ravines located at the test area 1(the red line in Fig. 2 indicates the location of this profile). The points represented in magenta correspond to the lidar-derived DEM (see section 2.3), while the red points take part of the DEM filtered from the PCI DSM (see section 3.3).

Conclusions

In this work it is proposed a methodological pipeline to automatically produce valuable 3D information (DSM and bare-earth DEM geospatial products) from VHR stereo imagery in order to potentially improve PCG mapping over large areas. Lidar derived DSM and DEM were used to carry out the vertical accuracy assessment of the stereo photogrammetrically generated products. Note that, to the best of our knowledge, this is the first work that addresses the challenge of the generation of DSM and DEM products in dense PCG areas from VHR satellite imagery. The way to merge this 3D geospatial information and the traditional 2D spectral-based information will be faced in further works.

With regards to DSM completeness, the RSP approach yielded significantly better scores than PCI, above all in high dense PCG areas, demonstrating that semi-global matching can extract image matching points even over radiometrically difficult-to-match image patches (e.g. some greenhouse roofs with a pronounced glint effect). This advantage turns out to be very relevant when dealing with generating DSM in very dense PCG areas.

Concerning vertical accuracy of the GMRF DSM, both PCI and RSP methods yielded similar vertical accuracy results in terms of random errors, with standard deviations ranging from 0.56 to 0.82 m. It must be underlined that a slightly higher positive bias (height overestimation) was detected in the case of RSP as compared to PCI, likely because RSP can incur a commission error when working on difficult to match image patches to achieve higher completeness scores than PCI.

The DEM error figures also showed no significant differences between the two tested approaches regarding random errors, presenting standard deviations ranging from 1.16 to 2.28 m. In relation to the systematic errors, they were much higher than those obtained in the case of GMRF DSM production, again RSP method showing a slightly higher bias than PCI. Summing up, the computed DEM error figures were highly dependent on DSM-to-DEM filtering error, in turn closely related to greenhouse density and terrain complexity. Concerning DSM-to-DEM automatic filtering, the PCI algorithm DEM2DTM usually yielded reasonable results, especially considering that only two parameters were tuned during a trial and error process. However, more spatially adapted parameters would be required to improve the final DSM-to-DEM filtering results. In this sense, it can be concluded that more research should be devoted to improving the filtering tools available to automatically convert a stereo photogrammetrically derived DSM into a bare-earth DEM in the case of PCG areas.

The 3D information provided through the methodological pipeline described in this work could be very valuable as a complement to the traditional 2D spectral information offered by VHR satellite imagery to improve PCG mapping and monitoring over large areas. This might be accomplished, for example, by computing the normalized digital surface model from the difference between the GMRF DSM and the corresponding DEM to obtain a georeferenced raster layer containing the height of all overlying objects on the terrain, such as buildings, trees and greenhouses.

Acknowledgements

This work was supported by the research projects “GreenhouseSat” (Grant Reference AGL2014-56017-R) and “Sentinel-GH” (Grant Reference RTI2018-095403-B-I00) funded by the Spanish National Plan for Research and the European Union ERDF funds. It also takes part of the general research lines promoted by the Agrifood Campus of International Excellence ceiA3 (http://www.ceia3.es/en). The kind comments and valuable suggestions made by anonymous reviewers are also very appreciated..

References:

Aguilar, F.J., Aguilar, M.A., Blanco, J.L., Nemmaoui, A., García Lorca, A., 2016. Analysis and Validation of Grid Dem Generation Based on Gaussian Markov Random Field. ISPRS - Int. Arch. Photogramm. Remote Sens. Spat. Inf. Sci. XLI-B2, 277–284. https://doi.org/10.5194/isprs-archives-XLI-B2-277-2016

Aguilar, F.J., Carvajal, F., Aguilar, M.A., Agüera, F., 2007. Developing digital cartography in rural planning applications. Comput. Electron. Agric. 55, 89–106. https://doi.org/10.1016/J.COMPAG.2006.12.008

Aguilar, F.J., Mills, J.P., 2008. Accuracy assessment of lidar-derived digital elevation models. Photogramm.

Rec. 23, 148–169. https://doi.org/10.1111/j.1477-9730.2008.00476.x

Aguilar, M.A., Agüera, F., Aguilar, F.J., Carvajal, F., 2008. Geometric accuracy assessment of the orthorectification process from very high resolution satellite imagery for Common Agricultural Policy purposes. Int. J. Remote Sens. 29, 7181–7197. https://doi.org/10.1080/01431160802238393

Aguilar, M.A., Bianconi, F., Aguilar, F.J., Fernández, I., 2014a. Object-Based Greenhouse Classification from GeoEye-1 and WorldView-2 Stereo Imagery. Remote Sens. 6, 3554–3582. https://doi.org/10.3390/rs6053554

Aguilar, M.A., Montalbán, M.A., Saldaña, M. del M., Aguilar, F.J., Fernández, I., García Lorca, A., 2014b. Detección remota de invernaderos a partir de estéreo pares del satélite WorldView-2. Rev. Teledetección 0, 19. https://doi.org/10.4995/raet.2014.2288

Aguilar, M.A., Nemmaoui, A., Aguilar, F.J., Novelli, A., García Lorca, A., 2017. Improving georeferencing accuracy of Very High Resolution satellite imagery using freely available ancillary data at global coverage. Int. J. Digit. Earth 10. https://doi.org/10.1080/17538947.2017.1280549

Aguilar, M.A., Nemmaoui, A., Novelli, A., Aguilar, F.J., García Lorca, A., 2016. Object-Based Greenhouse Mapping Using Very High Resolution Satellite Data and Landsat 8 Time Series. Remote Sens. 8, 1–19. https://doi.org/10.3390/rs8060513

Aguilar, M.A., Saldaña, M. del M., Aguilar, F.J., 2014b. Generation and quality assessment of stereo-extracted DSM from geoeye-1 and worldview-2 imagery. IEEE Trans. Geosci. Remote Sens. 52, 1259–1271. https://doi.org/10.1109/TGRS.2013.2249521

Aguilar, M.A., Saldaña, M. del M., Aguilar, F.J., 2013. Assessing geometric accuracy of the orthorectification process from GeoEye-1 and WorldView-2 panchromatic images. Int. J. Appl. Earth Obs. Geoinf. 21, 427–435. https://doi.org/10.1016/J.JAG.2012.06.004

Aguilar, M.A., Vallario, A., Aguilar, F., García Lorca, A., Parente, C., 2015. Object-Based Greenhouse Horticultural Crop Identification from Multi-Temporal Satellite Imagery: A Case Study in Almeria, Spain. Remote Sens. 7, 7378–7401. https://doi.org/10.3390/rs70607378

Aguilar, M.A., Nemmaoui, A., Aguilar, F.J., Rongjun Qin, R., 2018. Quality assessment of digital surface models extracted from WorldView-2 and WorldView-3 stereo pairs over different land covers, GIScience & Remote Sens. https://doi.org/10.1080/15481603.2018.1494408

Alobeid, A., Jacobsen, K., Heipke, C., 2010. Comparison of Matching Algorithms for DSM Generation in Urban Areas from Ikonos Imagery. Photogramm. Eng. Remote Sens. 76, 1041–1050. https://doi.org/10.14358/PERS.76.9.1041

Arefi, H., Reinartz, P., 2013. Building Reconstruction Using DSM and Orthorectified Images. Remote Sens. 5, 1681–1703. https://doi.org/10.3390/rs5041681

Åstrand, P.J., Bongiorni, M., Crespi, M., Fratarcangeli, F., Da Costa, J.N., Pieralice, F., Walczynska, A., 2012. The potential of WorldView-2 for ortho-image production within the “Control with Remote Sensing Programme” of the European Commission. Int. J. Appl. Earth Obs. Geoinf. 19, 335–347. https://doi.org/10.1016/J.JAG.2012.06.003

Barbarella, M., Fiani, M., Zollo, C., 2017. Assessment of DEM derived from very high-resolution stereo satellite imagery for geomorphometric analysis. Eur. J. Remote Sens. 50, 534–549. https://doi.org/10.1080/22797254.2017.1372084

Butler, J.B., Lane, S.N., Chandler, J.H., 1998. Assessment of Dem Quality for Characterizing Surface Roughness Using Close Range Digital Photogrammetry. Photogramm. Rec. 16, 271–291. https://doi.org/10.1111/0031-868X.00126

Büyüksalih, G., Jacobsen, K., 2007a. Comparison of DEM Generation by Very High Resolution Optical Satellites, in: Z. Bichenek (Ed.), New Developments and Challenge in Remote Sensing. Millpress, Rotterdam, Netherlands, p. 730.

Büyüksalih, G., Jacobsen, K., 2007b. Digital Surface Models in Build up Areas Based on Very High Resolution Space Images. Proceeding ASPRS 2007 Annu. Conf. 07-11 May 10 pages (on 2007 Annual Technical Papers CD-ROM).

Capaldo, P., Crespi, M., Fratarcangeli, F., Nascetti, A., Pieralice, F., 2012a. DSM generation from high resolution imagery: applications with WorldView-1 and GeoEye-1. Ital. J. Remote Sens. 44, 41–53. https://doi.org/10.5721/ItJRS20124414

Capaldo, P., Crespi, M., Fratarcangeli, F., Nascetti, A., Pieralice, F., Agugiaro, G., Poli, D., Remondino, F., 2012b. DSM generation from optical and SAR high resolution satellite imagery: Methodology, problems and potentialities, in: Piscataway, N.I. (Ed.), 2012 IEEE International Geoscience and Remote Sensing Symposium (IGARSS), 2012 IEEE International. New York, USA, pp. 6936–6939. https://doi.org/10.1109/IGARSS.2012.6352567

Celik, S., Koc-San, D., 2018. Greenhouse Detection Using Aerial Orthophoto and Digital Surface Model, in: De Pietro, G., Gallo, L., Howlett, R.J., Jain, L.C. (Eds.), Intelligent Interactive Multimedia Systems and Services 2017 (KES-IIMSS 2017). Springer International Publishing, Cham, pp. 51–59. https://doi.org/10.1007/978-3-319-59480-4_6

Cheng, P., 2015. Pan-sharpening, DEM Extraction and Geometric Correction - SPOT-6 and SPOT-7 Satellites. GeoInformatics 18, 24–27.

D ’angelo, P., Lehner, M., Krauss, T., Hoja, D., Reinartz, P., 2008. Towards Automated DEM Generation from High Resolution Stereo Satellite Images. Int. Arch. Photogramm. Remote Sens. Spat. Inf. Sci. 37, 1137–1142.

Daniel, C., Tennant, K., 2001. DEM Quality Assessment, in: (D. F. Maune, Editor), A.S.F.P. and R.S. (Ed.), Digital Elevation Model Technologies and Applications: The DEM Users Manual. Bethesda, Maryland, pp. 395–440.

de Franchis, C., Meinhardt-Llopis, E., Michel, J., Morel, J.-M., Facciolo, G., 2014. An automatic and modular stereo pipeline for pushbroom images. ISPRS Ann. Photogramm. Remote Sens. Spat. Inf. Sci. II-3, 49–56. https://doi.org/10.5194/isprsannals-II-3-49-2014

DeWitt, J.D., Warner, T.A., Chirico, P.G., Bergstresser, S.E., 2017. Creating high-resolution bare-earth digital elevation models (DEMs) from stereo imagery in an area of densely vegetated deciduous forest using combinations of procedures designed for lidar point cloud filtering. GIScience Remote Sens. 54, 552–572. https://doi.org/10.1080/15481603.2017.1295514

Di Rita, M., Nascetti, A., Crespi, M., 2017. Open source tool for DSMs generation from high resolution optical satellite imagery: development and testing of an OSSIM plug-in. Int. J. Remote Sens. 38, 1788–1808. https://doi.org/10.1080/01431161.2017.1288305

Dowman, I., 2000. Automatic feature extraction for urban landscape models. Adding value to Remotely Sensed Data. Proceedings of 26th Annual Conference of the Remote Sensing Society, in: Proceedings of the 26th Annual Conference of the Remote Sensing Society. Leicester , p. on CD-ROM.

Dowman, I., Jacobsen, K., Konecny, G., Sandau, R., 2012. High Resolution Optical Satellite Imagery, Whittles Publishing. Whittles Publishing, Scotland, UK.

Felicísimo, A.M., 1994. Parametric statistical method for error detection in digital elevation models. ISPRS J. Photogramm. Remote Sens. 49, 29–33. https://doi.org/10.1016/0924-2716(94)90044-2

Fratarcangeli, F., Murchio, G., Di Rita, M., Nascetti, A., Capaldo, P., 2016. Digital surface models from ZiYuan-3 triplet: performance evaluation and accuracy assessment. Int. J. Remote Sens. 37, 3505–3531. https://doi.org/10.1080/01431161.2016.1192308

Garnaud, J.C., 2000. Plasticulture : bulletin du comité international des plastiques en agriculture. Plast. 119, 30–43.

Ghuffar, S., 2016. Satellite Stereo Based Digital Surface Model Generation Using Semi Global Matching in Object and Image Space. ISPRS Ann. Photogramm. Remote Sens. Spat. Inf. Sci. III-1, 63–68. https://doi.org/10.5194/isprs-annals-III-1-63-2016

Grodecki, J., Dial, G., 2003. Block Adjustment of High-Resolution Satellite Images Described by Rational Polynomials. Photogramm. Eng. Remote Sens. 69, 59–68. https://doi.org/10.14358/PERS.69.1.59

Hirschmuller, H., 2008. Stereo Processing by Semiglobal Matching and Mutual Information. IEEE Trans. Pattern Anal. Mach. Intell. 30, 328–341. https://doi.org/10.1109/TPAMI.2007.1166

Hobi, M.L., Ginzler, C., 2012. Accuracy Assessment of Digital Surface Models Based on WorldView-2 and ADS80 Stereo Remote Sensing Data. Sensors 12, 6347–6368. https://doi.org/10.3390/s120506347

Höhle, J., Potuckova, M., 2006. The EuroSDR Test "Checking and Improving of Digital Terrain Models", in: European Spatial Data Research. Gopher, Utrecht, The Netherlands, pp. 9–141.

Jacobsen, K., 2006. Digital Surface Models of City Areas by Very High Resolution Space Imagery, in: The 1st EARSeL-Workshop on Urban Remote Sensing. p. 10 pages (on CD-ROM).

Lanorte, A., De Santis, F., Nolè, G., Blanco, I., Loisi, R.V., Schettini, E., Vox, G., 2017. Agricultural plastic waste spatial estimation by Landsat 8 satellite images. Comput. Electron. Agric. 141, 35–45. https://doi.org/10.1016/J.COMPAG.2017.07.003

Levin, N., Lugassi, R., Ramon, U., Braun, O., Ben-Dor, E., 2007. Remote sensing as a tool for monitoring plasticulture in agricultural landscapes. Int. J. Remote Sens. 28, 183–202. https://doi.org/10.1080/01431160600658156

Li, Z., Zhu, Q., Gold, C., 2005. Digital terrain modeling : principles and methodology. CRC Press, Boca Raton, Florida.

Luethje, F., Tiede, D., Eisank, C., 2017. Terrain Extraction in Built-Up Areas from Satellite Stereo-Imagery-Derived Surface Models: A Stratified Object-Based Approach. ISPRS Int. J. Geo-Information 6, 1–13. https://doi.org/10.3390/ijgi6010009

Ministerio de Fomento de España, 2015. Plan Nacional de Ortofotografía Aérea [WWW Document]. Especificaciones técnicas_ LiDAR 2015_Versión 150015. URL http://pnoa.ign.es/especificaciones-tecnicas (accessed 6.19.17).

Mokarram, M., Hojati, M., 2017. Morphometric analysis of stream as one of resources for agricultural lands irrigation using high spatial resolution of digital elevation model (DEM). Comput. Electron. Agric. 142, 190–200. https://doi.org/10.1016/J.COMPAG.2017.09.001

Muller, J.-P., Ourzik, C., Kim, T., Dowman, I., 1997. Assessment of the Effects of Resolution on Automated DEM and Building Extraction, in: Automatic Extraction of Man-Made Objects from Aerial and Space Images (II). Birkhäuser Basel, Basel, pp. 233–242. https://doi.org/10.1007/978-3-0348-8906-3_23

Noh, M.-J., Howat, I.M., 2017. The Surface Extraction from TIN based Search-space Minimization (SETSM) algorithm. ISPRS J. Photogramm. Remote Sens. 129, 55–76. https://doi.org/10.1016/J.ISPRSJPRS.2017.04.019

Noh, M.-J., Howat, I.M., 2015. Automated stereo-photogrammetric DEM generation at high latitudes: Surface Extraction with TIN-based Search-space Minimization (SETSM) validation and demonstration over glaciated regions. GIScience Remote Sens. 52, 198–217. https://doi.org/10.1080/15481603.2015.1008621

Novelli, A., Aguilar, M.A., Nemmaoui, A., Aguilar, F.J., Tarantino, E., 2016. Performance evaluation of object based greenhouse detection from Sentinel-2 MSI and Landsat 8 OLI data: A case study from Almería (Spain). Int. J. Appl. Earth Obs. Geoinf. 52, 403–411. https://doi.org/10.1016/J.JAG.2016.07.011

PCI Geomatics, 2016. Software User's Manual, PCI Geomatics Enterprises Inc., Richmond Hill. Canada.

Poli, D., Caravaggi, I., 2012. Digital surface modelling and 3D information extraction from spaceborne very high resolution stereo pairs : photogrammetric processing of stereo imagery over large metropolitan areas for global security and crisis management. Publications Office of the European Union, Luxembourg. https://doi.org/10.2788/15526

Poli, D., Remondino, F., Angiuli, E., Agugiaro, G., 2015. Radiometric and geometric evaluation of GeoEye-1, WorldView-2 and Pléiades-1A stereo images for 3D information extraction. ISPRS J. Photogramm. Remote Sens. 100, 35–47. https://doi.org/10.1016/J.ISPRSJPRS.2014.04.007

Qin, R., 2016. RPC Stereo Processor (RSP) - A software package for digital surface model and orthophoto generation from satellite stereo imagery. ISPRS Ann. Photogramm. Remote Sens. Spat. Inf. Sci. III-1, 77–82. https://doi.org/10.5194/isprs-annals-III-1-77-2016

Qin, R., 2014. Change detection on LOD 2 building models with very high resolution spaceborne stereo imagery. ISPRS J. Photogramm. Remote Sens. 96, 179–192. https://doi.org/10.1016/J.ISPRSJPRS.2014.07.007

Quintas-Soriano, C., Castro, A.J., Castro, H., García-Llorente, M., 2016. Impacts of land use change on ecosystem services and implications for human well-being in Spanish drylands. Land use policy 54, 534–548. https://doi.org/10.1016/J.LANDUSEPOL.2016.03.011

Reinartz, P., Tian, J., Arefi, H., Krauss, T., Kuschk, G., Partovi, T., D 'angelo, P., 2014. Advances in DSM Generation and Higher Level Information Extraction from High Resolution Optical Stereo Satellite Data, in: 34th Earsel Symposium, European Remote Sensing - New Opportunities for Science and Practice. p. 10 pages (on CD-ROM). https://doi.org/10.12760/03-2014-21

Seeruttun, S., Crossley, C.P., 1997. Use of digital terrain modelling for farm planning for mechanical harvest of sugar cane in Mauritius. Comput. Electron. Agric. 18, 29–42. https://doi.org/10.1016/S0168-1699(97)00017-3

Shean, D.E., Alexandrov, O., Moratto, Z.M., Smith, B.E., Joughin, I.R., Porter, C., Morin, P., 2016. ISPRS Journal of Photogrammetry and Remote Sensing An automated , open-source pipeline for mass production of digital elevation models (DEMs) from very-high-resolution commercial stereo satellite imagery. ISPRS J. Photogramm. Remote Sens. 116, 101–117. https://doi.org/10.1016/j.isprsjprs.2016.03.012

Sohn, G., Dowman, I., 2007. Data fusion of high-resolution satellite imagery and LiDAR data for automatic building extraction. ISPRS J. Photogramm. Remote Sens. 62, 43–63. https://doi.org/10.1016/J.ISPRSJPRS.2007.01.001

Tack, F., Goossens, R., Buyuksalih, G., 2009. Semi-automatic city model extraction from tri-stereoscopic VHR satellite imagery. Int. Arch. Photogramm. Remote Sens. Spat. Inf. Sci. 38, 89–96.

Tarantino, E., Figorito, B., 2012. Mapping Rural Areas with Widespread Plastic Covered Vineyards Using True Color Aerial Data. Remote Sens. 4, 1913–1928. https://doi.org/10.3390/rs4071913

Tian, J., Cui, S., Reinartz, P., 2014. Building Change Detection Based on Satellite Stereo Imagery and Digital Surface Models. IEEE Trans. Geosci. Remote Sens. 52, 406–417. https://doi.org/10.1109/TGRS.2013.2240692

Tomas, L., Fonseca, L., Almeida, C., Leonardi, F., Pereira, M., 2016. Urban population estimation based on residential buildings volume using IKONOS-2 images and lidar data. Int. J. Remote Sens. 37, 1–28. https://doi.org/10.1080/01431161.2015.1121301

Tong, X., Liu, S., Weng, Q., 2010. Bias-corrected rational polynomial coefficients for high accuracy geo-positioning of QuickBird stereo imagery. ISPRS J. Photogramm. Remote Sens. 65, 218–226. https://doi.org/10.1016/J.ISPRSJPRS.2009.12.004

Toutin, T., 2006a. Generation of DSMs from SPOT-5 in-track HRS and across-track HRG stereo data using spatiotriangulation and autocalibration. ISPRS J. Photogramm. Remote Sens. 60, 170–181. https://doi.org/10.1016/J.ISPRSJPRS.2006.02.003

Toutin, T., 2006b. Comparison of 3D Physical and Empirical Models for Generating DSMs from Stereo HR Images. Photogramm. Eng. Remote Sens. 72, 597–604. https://doi.org/10.14358/PERS.72.5.597

Toutin, T., 2002. Three-dimensional topographic mapping with ASTER stereo data in rugged topography.

IEEE Trans. Geosci. Remote Sens. 40, 2241–2247. https://doi.org/10.1109/TGRS.2002.802878

Toutin, T., Chenier, R., Carbonneau, Y., 2001. 3D geometric modeling of ikonos GEO images, in: In Proc. Joint ISPRS Workshop “High Resolution Mapping from Space. Hannover, Germany, pp. 1–9.

Weidner, U., Förstner, W., 1995. Towards automatic building extraction from high-resolution digital elevation models. ISPRS J. Photogramm. Remote Sens. 50, 38–49. https://doi.org/10.1016/0924-2716(95)98236-S

Wenzel, K., Rothermel, M., Haala, N., Fritsch, D., 2013. SURE - The ifp Software for Dense Image Matching, in: Fritsch Wichmann D. (Ed.), Photogrammetric Week. Berlin, pp. 59–70.

Wu, C., Deng, J.S., Wang, K., Ma, L.G., Tahmassebi, A.R.S., 2016. Object-based classification approach for greenhouse mapping using Landsat-8 imagery. IInternational J. Agric. Biol. Eng. 9, 79–88. https://doi.org/10.3965/j.ijabe.20160901.1414

Yang, D., Chen, J., Zhou, Y., Chen, X., Chen, X., Cao, X., 2017. Mapping plastic greenhouse with medium spatial resolution satellite data: Development of a new spectral index. ISPRS J. Photogramm. Remote Sens. 128, 47–60. https://doi.org/10.1016/J.ISPRSJPRS.2017.03.002

Zhang, L., Gruen, A., 2006. Multi-image matching for DSM generation from IKONOS imagery. ISPRS J. Photogramm. Remote Sens. 60, 195–211. https://doi.org/10.1016/J.ISPRSJPRS.2006.01.001

Zhang, Q., Qin, R., Huang, X., Fang, Y., Liu, L., 2015. Classification of Ultra-High Resolution Orthophotos Combined with DSM Using a Dual Morphological Top Hat Profile. Remote Sens. 7, 16422–16440. https://doi.org/10.3390/rs71215840

Zhao, X., Guo, Q., Su, Y., Xue, B., 2016. Improved progressive TIN densification filtering algorithm for airborne LiDAR data in forested areas. ISPRS J. Photogramm. Remote Sens. 117, 79–91. https://doi.org/10.1016/J.ISPRSJPRS.2016.03.016

LIST OF TABLES

Table 1 Characteristics of the panchromatic band for the WV-2 stereo pair.

Product	*WV-2 Stereo Pair*	
Images	*WV-2 Image 1*	*WV-2 Image 2*
Acquisition Date	July 5, 2015	July 5, 2015
Acquisition Time (GTM)	11:02	11:03
Off-nadir View Angle	12.6°	24.6°
Collection Azimuth	59.2°	172.7°
Collected Col GSD (m)	0.488	0.519
Collected Row GSD (m)	0.480	0.584
Product Pixel Size (m)	0.5	0.5

Table 2 PCG landcover density and completeness scores for the DSM extracted from applying the RSP and PCI stereo-matching approaches.

	PCG landcover (%)	Completeness (%) RSP stereo-matching	Completeness (%) PCI stereo-matching
Test area 1	16.43	99.42	93.19
Test area 2	27.51	99.57	94.42
Test area 3	49.32	99.25	88.13
Test area 4	85.65	98.87	86.65

Table 3 Vertical accuracy assessment results for the GMRF DSM produced by the PCI and RSP stereo matching methods. Units expressed in meters.

Test areas	Test area 1		Test area 2		Test area 3		Test area 4	
Method	RSP	PCI	RSP	PCI	RSP	PCI	RSP	PCI
Mean error	0.15	0.05	0.19	0.06	0.28	0.01	0.32	0.35
Standard deviation	0.62	0.65	0.59	0.56	0.78	0.72	0.80	0.82
Maximum error	3.43	3.68	3.15	2.92	3.68	3.13	3.53	4.11
Minimum error	-3.15	-3.58	-2.64	-2.68	-3.10	-3.04	-2.92	-3.38
L95	1.35	1.55	1.35	1.34	1.97	1.86	1.96	2.10
L90	0.88	0.84	0.90	0.79	1.26	1.16	1.34	1.37

Table 4 Vertical accuracy assessment results for the DEM extracted from the DSM produced by the PCI and RSP stereo matching methods. Units expressed in meters.

Test area	Test area 1		Test area 2		Test area 3		Test area 4	
DEM derived from	RSP	PCI	RSP	PCI	RSP	PCI	RSP	PCI
Mean error	-1.28	-1.26	0.46	0.27	0.97	0.61	1.78	1.60
Standard deviation	2.28	2.00	1.41	1.36	1.16	1.21	1.35	1.44
Maximum error	6.20	5.61	5.22	4.72	4.73	4.57	5.84	5.95
Minimum error	-8.62	-8.08	-4.34	-4.16	-2.30	-3.28	-2.30	-3.74
L95	5.81	5.10	3.59	3.19	3.27	3.01	3.83	3.92
L90	4.90	4.13	2.90	2.72	2.83	2.54	3.51	3.46

List of figures

Fig. 1.
Location of the study site in the province of Almeria (Spain) and the four selected subareas as red rectangles. These subareas are characterized, in addition to PCG and bare soil, by dry ravines (1), vegetation (2) urban areas (3) and very high concentration of PCG (4). Coordinate System: WGS84 UTM Zone 30.

Fig. 2.

Lidar-derived grid format DSM and DEM for the four test areas. Left column: Lidar-derived DSM. Right column: Lidar-derived DEM. The red line (DEM test area 1 in the first row on the right) corresponds to the location of the profile represented in Fig. 7).

Fig. 3.
Stereo photogrammetrically derived DSM corresponding to the four test areas generated from PCI (left column) and RSP (right column).

Fig. 4. Influence of local radiometric dissimilarity on greenhouse plastic cover in relation to DSM completeness over the test area 4. The PAN images from WV2 stereo pair are shown above. DSM produced by PCI and RSP software packages are shown below. Blue ellipses highlight greenhouses presenting glint changes while yellow ellipses mark two greenhouses painted white. Matching problems in both DSM are presented in red colour.

Fig. 5.
Spatial distribution of residuals for the GMRF DSM corresponding to the four test areas generated from PCI (left column) and RSP (right column).

Fig. 6.
Spatial distribution of residuals for the DEM corresponding to the four test areas derived from PCI DSM (left column) and RSP DSM (right column).

Fig. 7.
Vertical profile crossing one of the dry ravines located at the test area 1(the red line in Fig. 2 indicates the location of this profile). The points represented in magenta correspond to the lidar-derived DEM (see section 2.3), while the red points take part of the DEM filtered from the PCI DSM (see section 3.3).

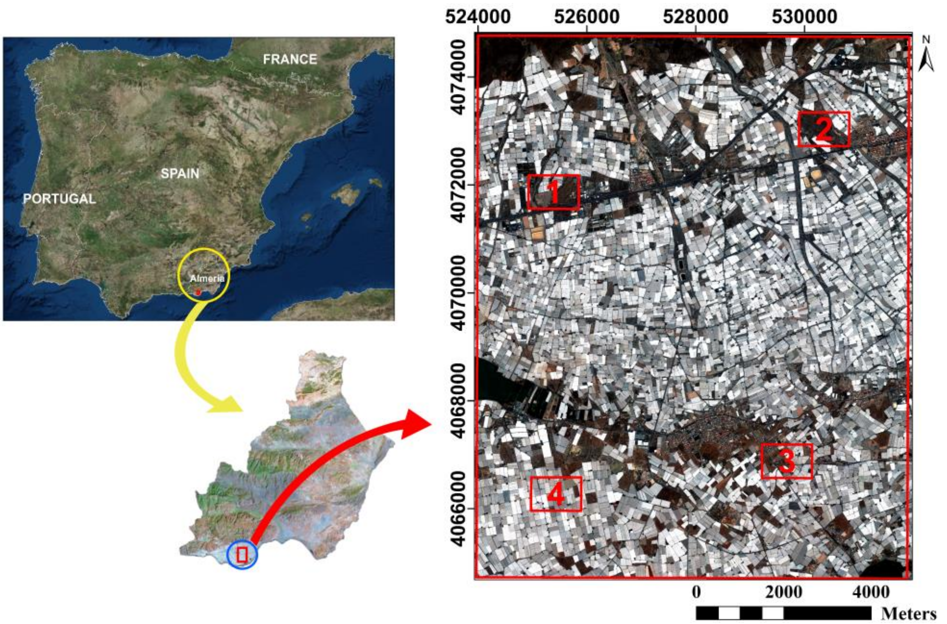

Fig. 1. Location of the study site in the province of Almeria (Spain) and the four selected subareas as red rectangles. These subareas are characterized, in addition to PCG and bare soil, by dry ravines (1), vegetation (2) urban areas (3) and very high concentration of PCG (4). Coordinate System: WGS84 UTM Zone 30.

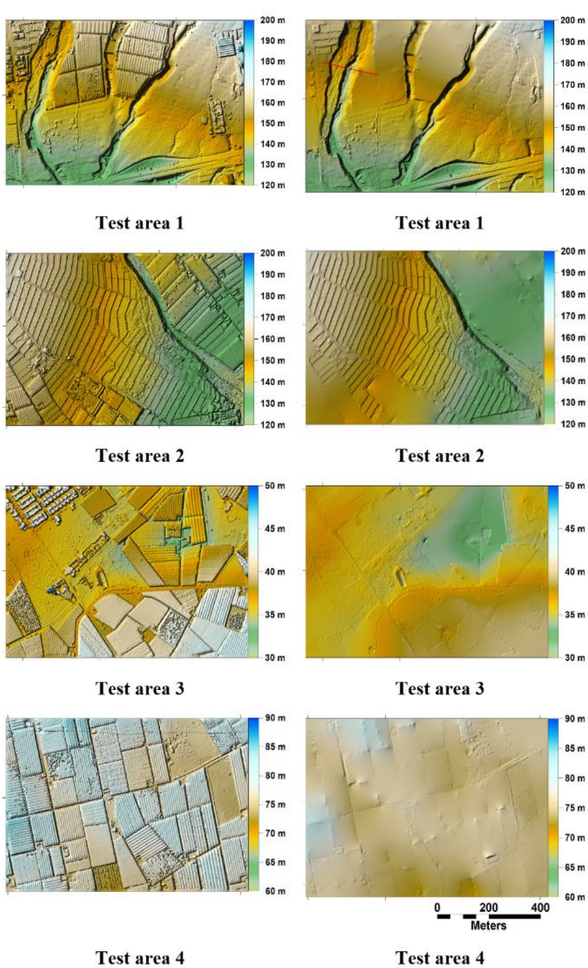

Fig. 2. Lidar-derived grid format DSM and DEM for the four test areas. Left column: Lidar-derived DSM. Right column: Lidar-derived DEM. The red line (DEM test area 1 in the first row on the right) corresponds to the location of the profile represented in Fig. 7).

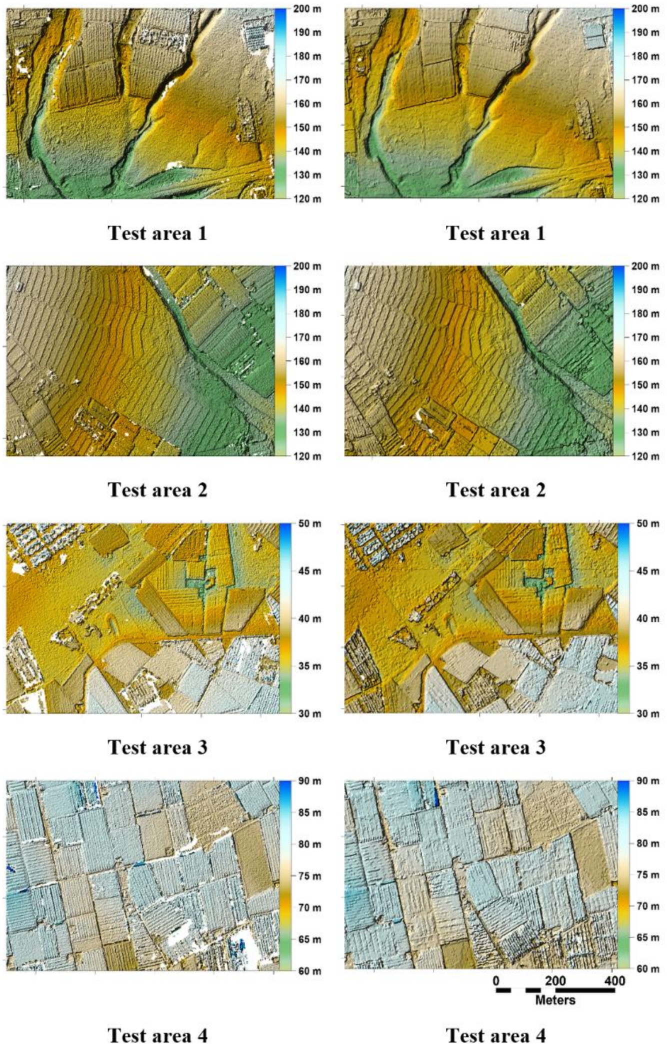

Fig. 3. Stereo photogrammetrically derived DSM corresponding to the four test areas generated from PCI (left column) and RSP (right column).

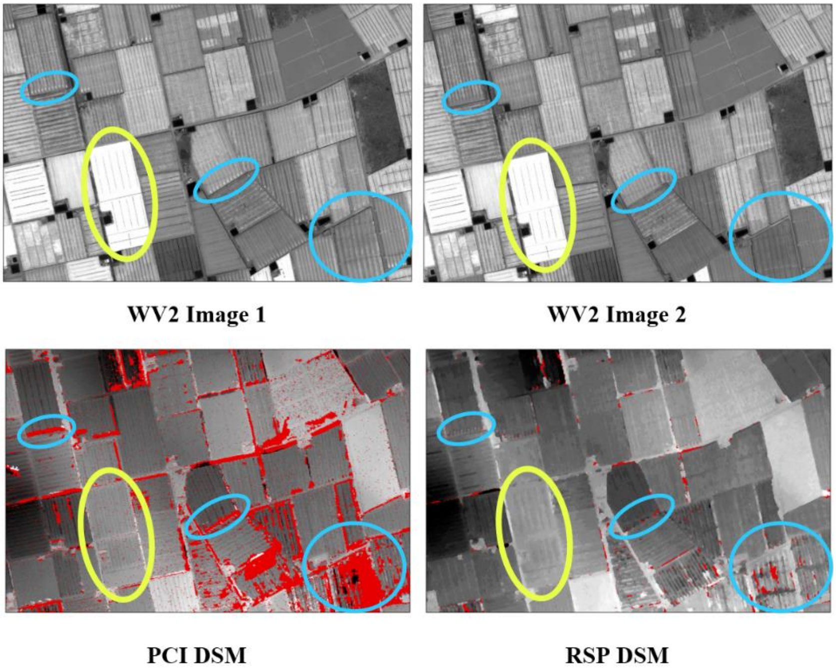

Fig. 4. Influence of local radiometric dissimilarity on greenhouse plastic cover in relation to DSM completeness over the test area 4. The PAN images from WV2 stereo pair are shown above. DSM produced by PCI and RSP software packages are shown below. Blue ellipses highlight greenhouses presenting glint changes while yellow ellipses mark two greenhouses painted white. Matching problems in both DSM are presented in red colour.

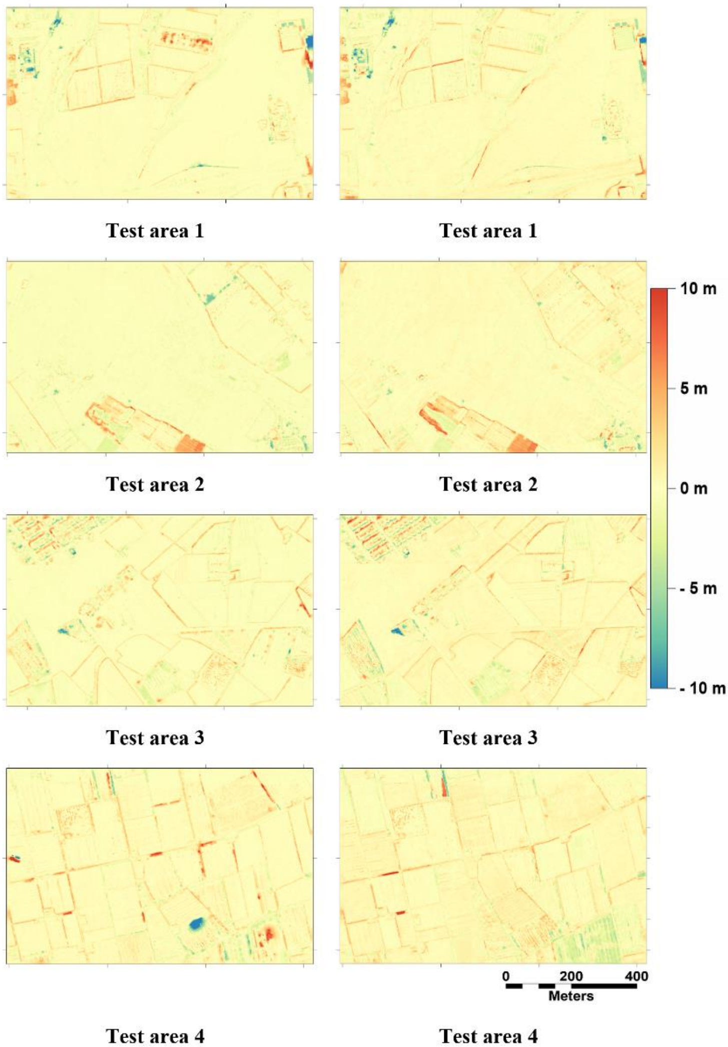

Fig.5. Spatial distribution of residuals for the GMRF DSM corresponding to the four test areas generated from PCI (left column) and RSP (right column).

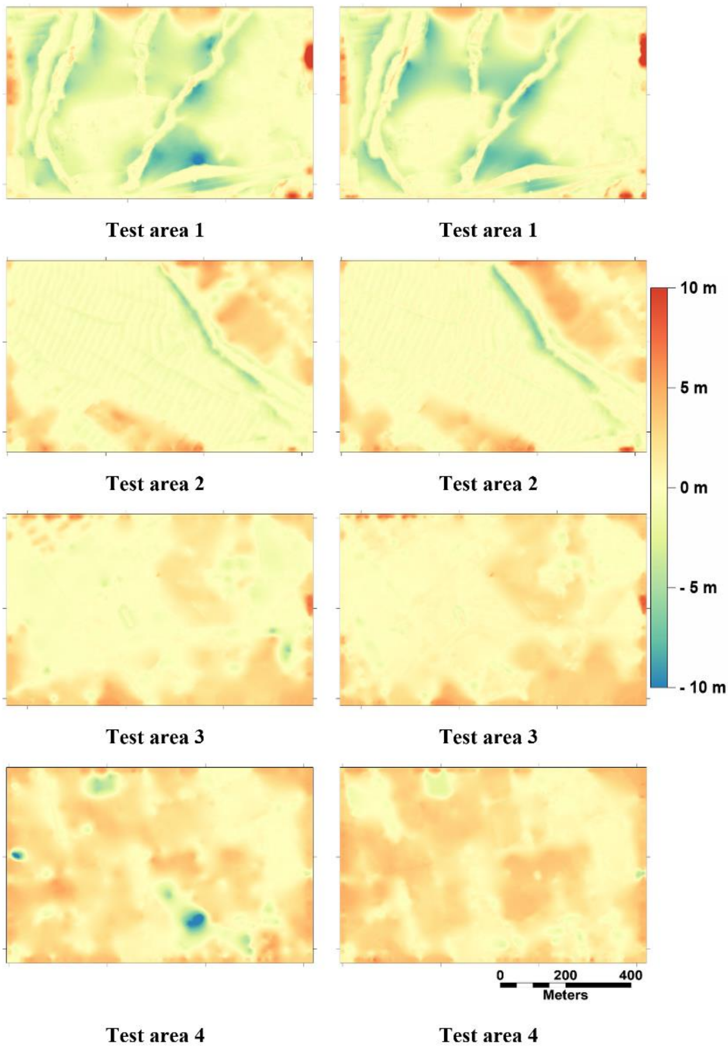

Fig. 6. Spatial distribution of residuals for the GMRF DEM corresponding to the four test areas derived from PCI DSM (left column) and RSP DSM (right column).

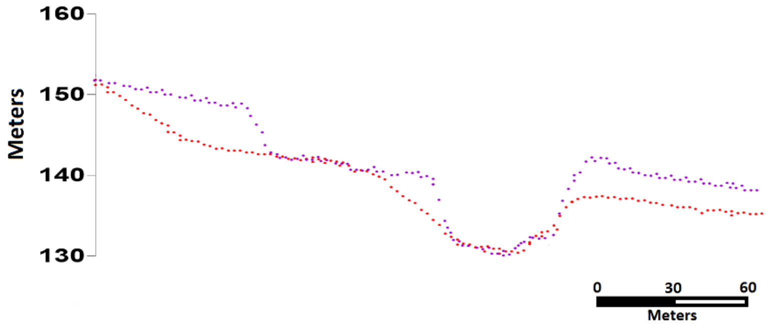

Fig. 7. Vertical profile crossing one of the dry ravines located at the test area 1(the red line in Fig. 2 indicates the location of this profile). The points represented in magenta correspond to the lidar-derived DEM (see section 2.3), while the red points take part of the DEM filtered from the PCI DSM (see section 3.3).